



American Society of
Mechanical Engineers

ASME Accepted Manuscript Repository

Institutional Repository Cover Sheet

ASME Paper Title: Construction and Experimental Study of an Elevation Linear Fresnel Reflector

Authors: Jonathan Nixon and Philip Davies

ASME Journal Title: Journal of Solar Energy Engineering

Volume/Issue 138 / 3

Date of Publication (VOR* Online) 23rd February 2016

ASME Digital Collection URL: <https://asmedigitalcollection.asme.org/solarenergyengineering/article-abstract/138/3/031001/379480/Construction-and-Experimental-Study-of-an?redirecte>

DOI: [10.1115/1.4032682](https://doi.org/10.1115/1.4032682)

ASME ©; CC-BY distribution license

*VOR (version of record)

Construction and Experimental Study of an Elevation Linear Fresnel Reflector

J. D. Nixon*

Aston University

Sustainable Environment Research Group, School of Engineering and Applied Science,
Aston Triangle, Birmingham, B4 7ET, UK

E-mail: j.nixon@kingston.ac.uk, Tel +44 (0)208 417 4727, present address: Kingston
University, Faculty of Science, Engineering and Computing, London, SW15 3DW, UK

*corresponding author

P. A. Davies

Aston University

Sustainable Environment Research Group, School of Engineering and Applied Science,
Aston Triangle, Birmingham, B4 7ET, UK

E-mail: p.a.davies@aston.ac.uk

Abstract

This paper outlines a novel elevation linear Fresnel reflector (ELFR) and presents and validates theoretical models defining its thermal performance. To validate the models, a series of experiments were carried out for receiver temperatures in the range of 30–100 °C to measure the heat loss coefficient, gain in heat transfer fluid (HTF) temperature, thermal efficiency and stagnation temperature. The heat loss coefficient was underestimated due to the model exclusion of collector end heat losses. The measured HTF temperature gains were found to have a good correlation to the model predictions – less than a 5% difference. In comparison to model predictions for the thermal efficiency and stagnation temperature, measured values had a difference of -39% to +31% and 22% to 38% respectively. The difference between measured and predicted values was attributed to the low temperature region for the experiments. It was concluded that the theoretical models are suitable for examining linear Fresnel reflector systems and can be adopted by other researchers.

Nomenclature

ΔT	Fluid temperature rise, K
A_a	Aperture area of concentrator, m ²
A_{cg}	Area of cover glazing, m ²
A_r	Area of receiver, m ²
C_p	Specific capacity of heat transfer fluid, kJ/kg.K
C_{pa}	Specific capacity of air, kJ/kg.K
d_c	Depth of cavity, m
D_i	Inside diameter of absorber pipe, m
D_o	Outside diameter of absorber pipe, m
F'	Collector efficiency factor
F''	Collector flow factor
F_R	Heat removal factor
g	Acceleration due to gravity, m ² /s
Gr	Grashof number
h_{co}	Convection heat transfer coefficient from outer cover glazing, W/m ² .K
h_{cp}	Convection heat transfer coefficient from absorber pipe, W/m ² .K
h_{fi}	Heat transfer coefficient inside absorber pipe, W/m ² .K
h_r	Height of receiver, m
h_{ro}	Radiation heat transfer coefficient from outer cover glazing, W/m ² .K
h_{rp}	Radiation heat transfer coefficient from absorber pipe, W/m ² .K
k_a	Thermal conductivity of air, W/m.K
k_{gw}	Thermal conductivity of insulation, W/m.K
k_{pipe}	Thermal conductivity of absorber pipe, W/m.K
L	Length of collector, m
L_{co}	Length of outer cover glazing, m
\dot{m}	Mass flow in solar field, kg/s
Nu_{co}	Nusselt number for convection from outer cover glazing
Nu_{cp}	Nusselt number for convection between absorber and cover glazing
Pr_{co}	Prandtl number for heat transfer from outer cover
Pr_{cp}	Prandtl number for heat transfer between absorber and cover glazing
Q_{in}	Heat transferred in, W
Q_u	Useful energy gained from solar field, W
Re	Reynold number

T_a	Ambient temperature, K
T_{avg}	Average temperature of absorber, K
T_c	Average temperature of cover glazing, K
T_{exit}	Exit fluid temperature from receiver, K
T_{in}	Inlet fluid temperature to receiver, K
T_p	Surface temperature of receiver's absorbing pipe, K
$T_{r,max}$	Stagnation temperature (maximum temperature of receiver), K
U_L	Heat transfer coefficient, W/m ² .K
U_{L1}	Heat loss through convection and radiation, W/m ² .K
U_{L2}	Heat loss through conduction, W/m ² .K
U_o	Overall heat loss coefficient, W/m ² .K

Greek Symbols

α_s	Solar altitude angle
β	Expansion coefficient of air, K ⁻¹
y_s	Azimuth angle from the south
ϵ_c	Emissivity of cover glazing
ϵ_p	Emissivity of absorber pipe
$\eta_{end-loss}$	Collector end-loss efficiency
$\eta_{o(0=\theta)}$	Optical efficiency at normal incidence
$\eta_{thermal}$	Thermal efficiency
θ_l	Transversal angle
θ_t	Longitudinal angle
μ	Dynamic viscosity of air, kg/m s
ν	Kinematic viscosity, m ² /s
ρ	Density of air, kg/m ³
σ	Stefan–Boltzman constant, 5.67 x 10 ⁻⁸ W/m ² .K ⁴

1 Introduction

The elevating linear Fresnel reflector (ELFR) is a new type of solar collector which, compared to the conventional linear Fresnel reflector (LFR), can provide a larger number of operating hours during the year using smaller land footprint. This is achieved through adjustable heights of the individual reflector elements to reduce shadowing and blocking of reflected rays, thus enabling improved optical collection, especially in the early and late hours of the day. The original conceptual design of the ELFR with a compound parabolic concentrator (CPC) cavity receiver was first described in an earlier paper by the same authors [1], but the practical realisation and test of the ELFR has not previously been reported. This paper, therefore, addresses the construction and experimental evaluation of the first ELFR prototype. A schematic of the ELFR is shown in Fig. 1.

The performance of LFRs and cavity receivers has been investigated by a number of authors using both experimental and modelling techniques which may be applied to the ELFR also. Singh et al. [2,3] studied the thermal efficiency and heat loss coefficient for an LFR trapezoidal cavity receiver with varying concentration ratios. They tested different receiver absorber coatings: black paint, bright nickel and black nickel. Electrical heaters were used to heat water in a storage tank. The water was then pumped through the receiver, and the flow rate was controlled with a regulator valve. The thermal efficiency was determined for different water inlet temperatures according to the ASHRAE standard-93 (1986), i.e. flow rate controlled to achieve a constant inlet and exit temperature for constant solar conditions. The heat loss coefficient was calculated by circulating Hytherm-500 oil at a constant flow rate for different inlet temperatures and measuring the difference in exit temperatures. An increase in mirror elements reduced the thermal efficiency and increased the settling time to reach stagnant temperature [4]. Khan [5] studied the heat loss coefficient and stagnation

temperature for an electroplated selective copper oxide coated absorber. Absorption was measured with an alpha meter. Emittance was measured with a thermopile, calibrated against a black body at 100 °C. Khan measured the heat loss by circulating heated water into the absorber at different steady state temperatures and measuring the steady state exit temperature. Negi et al. [6] evaluated the optical performance of black paint, selective cobalt oxide and selective MAXORB[®] foil as absorber coatings and also studied the heat loss coefficient for each coating. Flores Larsen et al. [7] also researched the heat loss characteristics of a trapezoidal cavity receiver, demonstrating a good correlation between experimental and theoretical results, and a good agreement with results reported by Singh et al, Khan and Negi et al. Yanhua et al. [8] analysed an LFR with CPC cavity receiver, finding the transmissivity of the cover glazing, reflectivity of the CPC and emissivity of the insulation to be the major influences on the receiver's thermal performance.

The thermal performance of cavity receivers has been characterised and optimised using computational fluid dynamic (CFD) techniques. With the aim of maximising thermal efficiency, Reynolds et al. [9] theoretically modelled the flow patterns of air in a trapezoidal cavity receiver using CFD and validated the results experimentally by photographing smoke patterns highlighted by quartz-halogen lights. They used electrical heaters to maintain a receiver temperature of 300 °C, and measured the heat loss from the power consumption. The National Renewable Energy Laboratory (NREL), U.S., applied a similar approach for measuring the heat loss of the Schott PTR70 receiver, which is currently used in most commercial parabolic trough and LFR power generating facilities. The heat loss coefficient in their experimental set-up was determined by heating the absorber pipe with electrical heaters placed inside a copper pipe centred in the absorber pipe. The power required to maintain the absorber pipe at a steady state temperature – measured with thermocouples – was then

recorded [10]. Facão and Oliveira [11] also applied CFD and ray-tracing techniques to optimise a trapezoidal cavity receiver for an LFR.

The optical properties of a receiver's absorbing surface have been the focus of many studies reported in the solar literature. The surface of a receiver requires a high solar radiation absorbance and low emissivity, with these properties remaining stable at high temperatures. Selectively coated surfaces, such as black nickel (NiS-ZnS) and stable nickel (Ni)-pigmented alumina (Al_2O_3), produced through electrolytic or chemical treatments are commonly used to achieve these properties [12]. A thin upper layer which is highly absorbent to shortwave solar radiation and transparent to longwave thermal radiation is deposited on a reflective surface with a low emissivity. Substrates typically used include aluminium and stainless steel. Konttinen et al. [13] characterized mechanically manufactured selective absorber surfaces using electron microscopy to determine surface groove width and a spectrometer to measure surface absorption and emissivity. A detailed review of solar absorber coatings has been reported by NREL [14].

The effects of mirror slope deviation errors and wind loads on solar thermal collectors have been examined. Heimsath et al. [15] used the Fringe Reflection Technique (FRT), a method used for measuring surface gradients, to investigate the optical characteristics of mirror elements in an LFR system. The FRT method requires a camera to record reflected patterns from a mirror, evaluating surface normals for each camera by phase measurement. They investigated various mirror elements and found a 1.2–4.5 mrad slope error from the ideal transversal slope, with maximum slope errors occurring at the edges of the mirrors. In the longitudinal plane, deviations were characterised by waviness. Mirrors fabricated for the Fresdemo project were also examined, and it was found that slope deviations caused by

torsion in mounting errors were greater than those caused by gluing. Heimsath et al. concluded that the slope errors observed are a typical characterisation of the mirror elements in an LFR, and that a Gaussian error distribution underestimates the mirror's optical quality due to the small statistical deviations in central areas. Due to the surface shape of the parabolic troughs and parabolic dishes, these collectors, rather than the LFR, have been at the focus of wind force studies [16-19].

The reviewed literature identifies the experimental procedures commonly applied for determining the performance of an LFR. Specific measured parameters include the heat loss coefficient, thermal efficiency and stagnation temperature. The experiments to determine these parameters can be summarised as: heat transfer fluid (HTF) heat loss for known mass flow (heat loss coefficient), HTF heat gain for known constant direct normal irradiance (DNI) and mass flow (thermal efficiency) and HTF maximum temperature for known DNI and zero mass flow (stagnation temperature).

The aims of this study were: (i) to construct a prototype ELFR and thus carry out experiments to verify theoretical models representing its performance and (ii) to demonstrate the ELFR in operation and thus learn about its performance and practical issues of implementation.

Theoretical models are presented in section 2 to estimate the heat loss coefficient, thermal efficiency and stagnation temperature, while models for optical efficiency were described in previous works by the authors [1,20]. Section 3 summarises the development and construction of the prototype ELFR system and section 4 describes a test set-up for performing the experiments. The experimental results enable comparisons to be drawn between measured and predicted results, and subsequently the validity of the theoretical models and the performance of the ELFR system are assessed.

2 Theory

2.1 Heat loss coefficient

The heat loss coefficient, U_L , for a cavity receiver can be estimated from the sum of the radiation and convection heat losses from an absorber pipe to cover glazing and the conduction losses from the insulated sides. One approach commonly adopted in the literature is to consider the losses between two horizontal plates – a method known as parallel plate correlation [2].

$$U_L = U_{L1} + U_{L2} \quad (1)$$

The heat loss from the bottom of the receiver through convection and radiation, U_{L1} , and conduction of the insulated sides, U_{L2} , is given by,

$$\frac{1}{U_{L1}} = \left[\frac{1}{h_{cp} + h_{rp}} + \left(\frac{A_r}{A_{cg}} \right) \left(\frac{1}{h_{co} + h_{ro}} \right) \right] \quad (2)$$

$$\frac{1}{U_{L2}} = \frac{1}{\left(\frac{k_{gw}}{A_r/L} \right)} \quad (3)$$

The heat loss from the absorber pipe to the cover glazing, h_{cp} , is calculated from,

$$h_{cp} = Nu_{cp} \cdot \frac{k_a}{d_c} \quad (4)$$

$$Nu_{cp} = 0.27 (Gr \cdot Pr_{cp})^{0.25} \quad (5)$$

$$Gr = \frac{\beta g (d_c)^3 (T_p - T_c)}{\nu^2} \quad (6)$$

$$Pr_{cp} = \frac{\mu C_{pa}}{k_a} \quad (7)$$

where Nu_{cp} is the Nusselt number for convection between the absorber and cover glazing, Pr_{cp} is the Prandtl number for heat transfer between the absorber and cover glazing, Gr is the Grashof number and d_c is the depth of the cavity. Other parameters include kinematic viscosity, ν , specific heat of air, C_{pa} , thermal conductivity, k_a , and expansion coefficient, β , which are taken for the average absorber pipe temperature, T_p . Eq.(7) is calculated using values for the average cover glazing temperature, T_c . The heat loss from the outer cover glazing, h_{co} , is given by,

$$h_{co} = Nu_{co} \cdot \frac{k_a}{L_{co}} \quad (8)$$

where,

$$Nu_{co} = 0.664 Re^{0.5} (Pr_{co})^{0.33} \quad (10^3 < Re < 2.6 \times 10^5) \quad (9)$$

$$Re = \rho \nu L / \mu \quad (10)$$

$$Pr_{co} = \mu C_{pa} / k_a \quad (11)$$

Parameters Nu_{co} and Pr_{cp} are, respectively, the Nusselt number for convection and the Prandtl number for heat transfer from the cover glazing. The Reynold number, Re , density, ρ , and

dynamic viscosity, μ , are determined for T_c and the ambient temperature, T_a . L_{co} is the length of the cover glazing. The radiation losses from the receiver, h_{ro} , and between the absorber pipe and cover glazing, h_{rp} , are determined from,

$$h_{ro} = \sigma \varepsilon_c (T_c^2 + T_a)(T_c + T_a) \quad (12)$$

$$h_{rp} = \frac{[\sigma(T_p^2 + T_c^2)(T_p + T_c)]}{\left[\left(\frac{1}{\varepsilon_c}\right) + \left(\frac{1}{\varepsilon_p}\right) - 1\right]} \quad (13)$$

Therefore, the heat loss coefficient can be estimated using assumptions or measurements for T_p , T_c , T_a , and the emissivity of the cover glazing, ε_c , and absorber pipe, ε_p .

The heat loss coefficient can be measured from an HTF losing energy to the ambient (temperature drop from receiver inlet, T_{in} , to exit T_{exit}) and travelling at a known mass flow rate, \dot{m} .

$$U_L = \frac{\dot{m}C_p(T_{in} - T_{exit})}{A_r(T_{avg} - T_a)} \quad (14)$$

The average fluid temperature, T_{avg} , is determined from,

$$T_{avg} = \frac{T_{in} + T_{exit}}{2} \quad (15)$$

2.2 Thermal efficiency

To predict the thermal efficiency of a solar collector, the exit fluid temperature for a given flow rate, needs to be calculated. This requires knowledge of the collector's flow characteristics, which can be modelled using a series of equations for the heat exchange or collector efficiency factor, F' , collector flow factor, F'' , and heat removal factor, F_R [21,22].

$$F' = \frac{U_o}{U_L} \quad (16)$$

$$U_o = \left(\frac{1}{U_L} + \frac{D_o}{h_{fi}D_i} + \frac{D_o \ln\left(\frac{D_o}{D_i}\right)}{2k_{pipe}} \right)^{-1} \quad (17)$$

$$F'' = \frac{\dot{m}C_p}{A_r U_L F'} \left[1 - \exp\left(-\frac{A_r U_L F'}{\dot{m}C_p}\right) \right] \quad (18)$$

$$F_R = F'' \cdot F' \quad (19)$$

Where D_i , D_o and k_{pipe} are respectively the inside diameter, outside diameter and thermal conductivity of the absorber pipe. The overall heat loss coefficient and heat transfer coefficient inside the pipe is notated respectively as U_o and h_{fi} .

The heat transferred to the receiver's absorbing pipe, Q_{in} , can be approximated by,

$$Q_{in} = DNI \cdot A_a \cdot \eta_{(\theta=0)} \cdot IAM(\theta_t, \theta_l) \cdot \eta_{end-loss} \quad (20)$$

The direct normal irradiance, DNI, is the energy available to the system. The ELFR's optical efficiency at normal incidence angle, $\eta_{(\theta=0)}$, (i.e. rays perpendicular to the effective aperture

area of the collector) and a bi-axial incidence angle modifier, $IAM(\theta_t, \theta_l)$, are defined in [1].

The IAM is based on incidence angle dependent optical losses (cosines losses for each mirror element, reflectance of mirror elements, transmittance of the cover glazing, reflectance of the secondary concentrator, absorbance of the receiver and an intercept factor). For an LFR, it also incorporates shadowing and blocking of reflected rays, although these losses are almost completely avoided by the ELFR. An LFR's IAM can be approximated by considering solar rays projected into two orthogonal planes: a longitudinal and transversal plane [23]. An overall IAM can be determined from a product of the angle modifiers for rays at a transversal angle, $IAM(\theta_t)$, and longitudinal angle, $IAM(\theta_l)$ [24].

The transversal and longitudinal angles from the vertical can be calculated from,

$$\theta_t = 90 - \tan^{-1} \left(\frac{\tan \alpha_s}{\cos(90 - \gamma_s)} \right) \quad (21)$$

$$\theta_l = 90 - \tan^{-1} \left(\frac{\tan \alpha_s}{\cos \gamma_s} \right) \quad (22)$$

where α_s and γ_s are respectively the altitude angle and azimuth angle from the south.

Eq. 23 and 24 are profiles for $IAM(\theta_t)$ and $IAM(\theta_l)$ obtained for the ELFR through ray-tracing [1]. The bi-axial incidence angle modifier, $IAM(\theta_t, \theta_l)$, using transversal and longitudinal angles in degrees, is determined from the product of these two equations.

$$IAM(\theta_t) = 0.00000012\theta_t^4 - 0.000021\theta_t^3 + 0.0012\theta_t^2 - 0.025\theta_t + 0.99 \quad (23)$$

$$IAM(\theta_l) = -0.000000065\theta_l^4 + 0.0000051\theta_l^3 - 0.00016\theta_l^2 + 0.00095\theta_l + 0.99 \quad (24)$$

The end-loss efficiency of the ELFR, $\eta_{end-loss}$, is considered as the collector prototype is only four metres in length. The end-loss can be found from the length of the collector, L , and height of the receiver, h_r ,

$$\eta_{end-loss} = 1 - \frac{h_r \tan \theta_l}{L} \quad (25)$$

Having determine the collector flow characteristics and heat transferred to the received, the fluid useful heat gain, Q_u , can be determined from,

$$Q_U = F_R A_a \left[Q_{in} - \frac{A_r}{A_a} U_L (T_{in} - T_a) \right] \quad (26)$$

where A_a is the concentrator's effective aperture area for a solar zenith angle of zero and A_r is the receiver's absorbing surface area.

The fluid temperature rise, ΔT , for a given mass flow rate is calculated from,

$$\Delta T = T_{in} - T_{exit} = \frac{Q_u}{\dot{m} C_p} \quad (27)$$

thus the exit temperature and subsequently the thermal efficiency can be predicted for a known useful heat gain and HTF mass flow rate. Moreover, the HTF mass flow rate can be controlled to achieve a desired exit temperature. Iterative calculations are required as the heat loss coefficient, mass flow rate and useful energy gain are dependent on each other. The thermal efficiency, $\eta_{thermal}$, is determined from,

$$\eta_{thermal} = \frac{\dot{m}C_p(T_{exit} - T_{in})}{DNI\eta_{endloss}A_a} \quad (28)$$

Measurement of the thermal efficiency enables the optical efficiency to be estimated for a predicted heat exchange efficiency factor as the thermal efficiency is also given by,

$$\eta_{thermal} = F' \left[\eta_{0(\theta=0)} IAM(\theta_t, \theta_l) - \frac{U_L A_r (T_{avg} - T_a)}{DNI \eta_{endloss} A_a} \right] \quad (29)$$

which can be rearranged to give,

$$\eta_{0(\theta=0)} IAM(\theta_t, \theta_l) = \frac{\eta_{thermal}}{F'} + \frac{U_L A_r (T_{avg} - T_a)}{DNI \cdot \eta_{endloss} A_a} \quad (30)$$

2.3 Stagnation temperature

The stagnation temperature is a useful parameter as it can be measured to enable estimated heat loss coefficient and optical efficiency values to be evaluated. The stagnation temperature, $T_{r,max}$, of the ELFR is estimated from [21],

$$T_{r,max} = T_a + \frac{DNI \cdot A_a \eta_{0(\theta=0)} \cdot IAM(\theta_t, \theta_l) \cdot \eta_{endloss}}{U_L A_r} \quad (31)$$

3 Development of the ELFR

The ELFR prototype was initially designed in a 3D computer aided design package and comprised three subassemblies: the frame, the concentrator elements and the CPC cavity receiver. The prototype was then built and installed on the roof of Aston University, Birmingham, UK. The details of the design and construction of the ELFR's frame,

concentrator elements and receiver are now individually discussed. The software tools used for design modelling, simulation and control are also described. Further details on the fabrication process of the prototype and the components used can be found in [25].

3.1 The frame

The 4.0 x 2.5 x 3.2 m frame was constructed from Item[®] Machine Building (MB) kit system [26], which comprised high tensile aluminium profiles and fastening elements. The MB kit was chosen for this project because of its assembly flexibility and modular nature, which overcame problems of restricted access and unavailability of welding and heavy lifting equipment. The frame was secured to withstand lift and tipping forces under wind speeds of 80 mph (36 m/s) – the maximum gust wind speed recorded in Birmingham, UK [27]. The receiver tower was tethered to the frame extremities using galvanised steel guy cables, which were sized according to expected cable tensions.

3.2 The concentrator elements

The mechanisms of the concentrator elements for the ELFR were designed to enable solar tracking by controlling the angle and height of the mirror elements. To protect the mirror coating and increase rigidity, marine plywood and aluminium profiles were glued to the back using sealant and construction adhesive. The mirror elements were then secured to the frame with polymer bearings. Each element row was rotated by a stepper motor and worm wheel assembly, which were placed inside IP 66 rated die cast aluminium enclosures. Elevation was achieved with a pair of LA35 linear actuators and a TR-EM-239 parallel drive unit [28]. Linear rails were used to keep the frame rigid. Address communication control boards for the stepper motor and actuator system were developed and placed inside the enclosures. The

motors were controlled through the use of a computer, a data acquisition device (DAQ), an encoder and decoders.

A tracking algorithm was developed to control the individual mirror element's angle and elevation. Each mirror element's slope angle and elevation height – to maintain focus on the receiver while avoiding shading and blocking – was determined sequentially from adjacent elements positions, geometrical position in respect to the receiver, site location (sun-earth geometry) and solar time.

With each additional mirror's contribution to the absorber surface decreasing – due to increased cosine losses, reduced effective aperture area, and limited range of elevation to remove blocking and shadowing – the number and width of the mirror elements were chosen as 8 and 250 mm, respectively. For mirror widths greater than 250 mm, curved mirrors would be required to avoid an oversized CPC receiver.

3.3 The CPC cavity receiver

The cavity receiver designed and implement for the ELFR comprised a secondary compound parabolic concentrator, three absorber pipes and a cover glazing. The CPC profile was formed from aluminium sections to support and shape a highly reflective stainless steel sheet (reflectivity $\approx 95\%$). The absorber pipes were aluminium coated in a lacquered dull black nickel (absorption $\approx 90\%$, emissivity ≈ 0.17) and the cover glazing was made from clear cast acrylic (transmittance $\approx 96\%$, emissivity ≈ 0.88) [14]. The absorber pipes were also insulated with a reflective insulation sheet and fibre glass wool. A cross section schematic of the CPC receiver is shown in Fig. 2.

The CPC was designed and positioned by calculating ray angles from the concentrator's extremities and the width of the focal point at the CPC aperture. The width of the focal point – referred to as the band of illumination, which comprises a central band of light from non-diverging rays and bands of light from diverging rays – can be calculated for a known number of mirror rows, with specified width and spacing, at a certain vertical distance from the target receiver [29]. For the prototype ELFR, the receiver height was limited to 2.5 m, and a CPC was designed to receive all rays approaching from the sun at the zenith. The final CPC parameters were a half acceptance angle of 32 degrees, a truncated aperture of 272 mm, a target width of 154 mm and a truncated height of 200 mm. The resulting average number of internal reflections for this CPC was found to be 1.4. The equations for designing a CPC are specified by Welford and Winston [30].

4 Experimental set-up

The ELFR was installed in a shadow-free location with a north-south axis east-west tracking orientation. Water was used as the HTF and was circulated through the three absorber pipe in series. The water circulation system included a 145 litre stainless steel direct open vented cylinder fitted with a 3 kW immersion heater and thermostat, 115 litre cold water header tank, Grundfos domestic circulating pump, 2-30 l/min turbine flow metre (+/-3% accuracy), steam hose, valves, copper pipes and pipe fittings. The receiver was fitted at the inlet and exit with pipe probe type K thermocouples (+/-1.0 °C accuracy). The set-up is delineated in Fig. 3. The temperature values and the mass flow rate were logged using a National Instrument® (NI) DAQ. To prevent pressure building up, vents were located before and after the receiver so that air could be removed from the system.

The DNI was measured using a pyrheliometer, which is the designated instrument by the International Standard ISO 9060 and the World Meteorological Organization (WMO) with which to measure direct solar radiation. The pyrheliometer used was Kipp and Zonen's CHP 1, and is an instrument compliant with ISO 9060, calibrated at the World Radiation Centre (WRC) in Switzerland.

5 Experimental procedure

Different HTF inlet temperatures were produced by preheating the water in the cylinder and controlling the thermostat; the inlet temperature was limited to a maximum temperature of 65 °C. The HTF flow rate was controlled and maintained by means of the ball valves and the pump's variable speed control. The fluid inlet and exit temperatures were recorded to determine when the system had stabilised and achieved a steady state. Average fluid temperatures were determined from Eq.(15). To measure the heat loss coefficient, the ELFR was not focused, i.e. zero solar input, and the steady state temperature drop from inlet to exit was recorded. The cover glazing and pipe temperatures were also measured with type K thermocouples. The pyrheliometer was used to measure the ambient temperature.

The thermal efficiency was measured for different HTF inlet temperatures. Steady state inlet and exit temperatures values were again recorded, this time with the ELFR focused (see Fig. 4) and experiments performed during approximately constant solar conditions. All experimental values were averaged over a period of steady state operation. The stagnation temperature was measured at solar noon with the pump turned off, valves closed and the collector having been focused for several hours to achieve a maximum stable receiver temperature. For safety reasons, the system was not pressurised; therefore, temperatures above 100 °C could not be achieved as at this point the HTF (water) boiled. To overcome this

difficulty when it occurred, only one-half of the collector's mirrors were focused, which resulted in a concentration ratio of 5 instead of 10.

6 Results: predictions and experimental measurements

6.1 Heat loss coefficient

In March a series of experiments were carried out to measure and estimate the ELFR's heat loss coefficient for average fluid temperatures in the range of 30–65 °C (see Fig. 5a-c). In this temperature range, the difficulty with measuring the heat loss was evident by widely varying results, ranging from 8.6 – 18.8 W/m².K (see Fig. 6). This is attributed to the low receiver temperatures, as small inaccuracies of the type K thermocouples and flow meter will have had a significant effect of the measured heat loss. Using the ambient and cover glazing temperature measurements the receiver's heat loss coefficient was estimated to increase from 2.9 – 3.42 W/m².K, which was a 66.3% to 81.8% decrease in comparison to the measured heat loss values (8.6 – 18.8 W/m².K).

6.2 Thermal efficiency

In March and May at varying times of day, a series of experiments were performed during relatively constant solar conditions (DNI variation of less than 50 W/m²) to measure the fluid temperature gain for different inlet temperatures. Measured values for the solar conditions, HTF mass flow, ambient, inlet and exit temperatures, thermal efficiency and derived optical efficiency are tabulated in Table 1. Fig. 7a–c shows example results for average fluid temperatures of 38 °C, 45 °C and 55 °C. For the same solar and inlet temperature conditions, and using the estimated heat loss coefficient and a ray-tracing model for an incident angle dependant optical efficiency described in [20], the HTF exit temperature and consequently

the thermal and optical efficiencies were predicted using the outlined flow characteristic equations presented in Section 2.2 (see Table 2).

Table 1: Measured HTF exit temperatures and resulting thermal efficiencies for the ELFR receiving varying DNI and HTF inlet temperatures. The IAM dependant optical efficiencies based on the measured thermal efficiencies and heat loss coefficients are also tabulated.

DNI W/m ²	θ_t °	θ_i °	U_L W/m ² .K	T_a °C	T_{in} °C	\dot{m} kg/s	T_{exit} °C	$\eta_{(\theta=0).IAM}$ %	$\eta_{thermal}$ %
668	47.2	48.7	8.12	13.0	15.8	0.12	19.5	71	70
682	9.6	49.4	7.99	17.2	37.7	0.15	39.3	61	59
798	38.7	49.4	8.03	21.9	41.1	0.14	43.3	52	50
839	2.8	50.2	8.00	18.3	45.1	0.14	46.9	55	52
743	30.3	49.2	8.01	18.8	48.5	0.15	50.4	53	50
812	21.4	31.1	7.94	24.4	52.7	0.41	53.5	33	31
814	41.6	49.8	8.06	20.5	54.5	0.15	57.2	55	52
576	52.3	48.4	7.97	19.4	61.4	0.17	62.6	36	32
726	63.4	48.7	8.02	20.3	63.5	0.15	72.6	63	49

Table 2: Predicted HTF exit temperatures and resulting thermal efficiencies for the ELFR receiving varying DNI and HTF inlet temperatures. The IAM dependant optical efficiencies based on a ray-tracing model and estimated heat loss coefficients are also tabulated.

DNI W/m ²	θ_t °	θ_i °	U_L W/m ² .K	T_a °C	T_{in} °C	\dot{m} kg/s	T_{exit} °C	$\eta_{(\theta=0).IAM}$ %	$\eta_{thermal}$ %
668	47.2	48.7	2.59	13.0	15.8	0.12	18.5	52	51
682	9.6	49.4	2.99	17.2	37.7	0.15	39.0	52	50
798	38.7	49.4	3.07	21.9	41.1	0.14	43.5	56	54
839	2.8	50.2	3.14	18.3	45.1	0.14	47.0	56	55
743	30.3	49.2	3.20	18.8	48.5	0.15	50.4	53	51
812	21.4	31.1	3.28	24.4	52.7	0.41	54.2	56	54
814	41.6	49.8	3.32	20.5	54.5	0.15	57.1	53	51
576	52.3	48.4	3.44	19.4	61.4	0.17	63.2	50	48
726	63.4	48.7	3.49	20.3	63.5	0.15	66.2	43	41

With a less than 5% deviation, predicted and measured HTF exit temperatures had a strong correlation (see Fig. 8). The difference between the measured and predicted thermal efficiency values was more substantial (-38.8% to +31.0%). Fig. 9 shows that in comparison

to the ray-tracing model prediction, the optical efficiency estimate (based on the thermal efficiency measurement) had a similar difference of -23.2% to +31.9%.

6.3 Stagnation temperature

In May from 8 a.m. to solar noon, an experiment was carried out with one-half of the ELFR receiving around 760 W/m^2 of DNI and pipe, inlet and exit temperature measurements recorded. Maximum temperatures of 80–90 °C were achieved at solar noon, thus indicating the ELFR's stagnation temperature (see Fig. 10). The fluctuating results seen in Fig. 10 were attributed to the temperature gradients between the bottom and top of the pipe, varying DNI, changing sun position (frame shadows and IAM) and the formation of bubbles as the water neared boiling point. In comparison, for the same solar conditions, the predicted stagnation temperature was 110 °C, i.e. a 22–38% increase in comparison to the measured stagnation temperature.

7 Discussion

Measured values for the heat loss coefficient indicated that the parallel plate correlation model underestimated the heat loss coefficient. This was most likely because the model did not take into account the receiver's end heat losses. Other authors have also reported experimental values 27–37% higher than those predicted by parallel plate correlation, and considered these error margins to be acceptable [2]. The estimated heat loss trend based on the average receiver, cover glazing and ambient temperatures demonstrated a good correlation (less than 10 % deviation) to those measured and estimated for similar receiver types by Singh et al. [2], Khan [5], Negi et al. [6] and Flores Larsen et al. [7].

Experimental measurements for the thermal efficiency and stagnation temperature had a reasonable agreement with the theoretical predictions. The thermal efficiency was determined by modelling and measuring the HTF (water) exit temperature. Measured values for the collector's HTF exit temperature correlated strongly with model predictions, giving only a -1% to +5% difference. However, due to the low temperature range of the experiments, this small error in temperature measurement had a significant effect on the deviation between the measured and predicted thermal efficiency (-38.8% to +31.0%) and, therefore, also the optical efficiency (-23.22% to +31.9%). The measured stagnation temperature was 18% to 27% lower than predicted values. This was attributed to the underestimated heat loss coefficient and an overestimated optical efficiency as the ray-tracing model did not take into account mirror surface shape errors, mirror degradation, accumulation of dirt on the cover glazing and mirrors, and tracking and alignment errors.

From the construction of the prototype it was learnt that one of the most difficult mechanics to achieve was a rigid and accurate method for rotating the mirror elements. The developed program and stepper motors used to drive the mirrors worked well; however, backlash and movement occurred in the worm and wheel assembly and bearings. The linear rails and actuators used for elevating the mirror elements performed well: precise (within +/- 0.4 mm) and rigid. The secondary CPC was shaped using multiple CPC profiled supports at 500 mm intervals; however, the mirror was fractionally distorted between the profiles. Though the MB kit was ideal for the prototype, faster installation and more cost effective materials would be required for a final product. For a final design, a receiver height of 5 m with a single absorber pipe would be used to reach a concentration ratio of 30, and thus higher temperatures will be achievable. The best coating is still an open problem with a range of materials and

manufacturing techniques available (e.g. spluttering and multi-layer selective and cement coatings).

In future studies, thermal oil (to perform experiments above 100 °C) and high precision flow rate and temperature measurement equipment should be used. Alternative absorber coatings that achieve low emissivity and high absorption properties at the ELFR's expected operating temperatures should be researched. The cavity receiver's heat loss coefficient and thermal efficiency could be optimised using CFD. The mirror slope surface errors could be investigated to develop a more accurate ray-tracing model for LFR systems. The number and width of mirror elements in an ELFR system should also be studied further to develop an optimum geometrical design to improve the cost effectiveness of the ELFR. The overall cost effectiveness of the ELFR and potential low and medium temperature applications for the technology have been discussed in [1].

8 Conclusion

An experimental set-up for measuring different performance parameters of a novel LFR system was described. Receiver temperatures were limited by a coupled tank-immersion heater and by the fact that the system was not pressurised. For receiver temperatures in the range of 30–65 °C, the estimated heat loss had a less than 10% deviation from results (estimated and measured) published by other authors on similar systems. Measured values for the HTF temperature gain, thermal efficiency (31–70%) and stagnation temperature (80–90 °C) had a difference from predicted values of -1% to 5%, -39% to +31% and 22% to 38% respectively. The estimated optical efficiency, based on the measured thermal efficiency and heat loss coefficient, had a percentage difference from a ray-tracing model of -23% to +32%.

It was concluded that the described theoretical models for determining the useful energy gained by an HTF were valid based on the experimental results for the heat loss coefficient, thermal efficiency and stagnation temperature. The deviation between the measured and predicted thermal efficiency results arose due to the low temperature range of the experiments and the prototype nature of the collector. For experiments conducted at higher temperatures, the impact of small errors – such as the -1% to 5% difference between measured and predicted HTF exit temperature – on the thermal efficiency deviation will be reduced, and the model is expected to have a closer agreement with experimental measurements.

It was further thought that this study can guide other researchers and manufacturers building and testing solar thermal collectors. In particular, the low-cost experimental set-up described can be easily replicated. As a result of the insights gained into the operating and design characteristics of the prototype ELFR, it was recommended that future LFR projects give careful consideration to the design of mirror elements to avoid backlash and bearing movement, choice of selective absorber coating and the method for forming a secondary CPC. We conclude that this study confirms the potential of the ELFR to extend operating hours and reduce the land footprint of the LFR, and therefore consider it to be a promising option for future LFR applications.

Acknowledgments

The authors would like to thank O. N. Igobo for his assistance in this study.

Funding

Science Bridge project financed by Research Councils UK (EP/G039992/1) and Department of Science and Technology, India.

Figure and table legends

- Fig. 1** Schematic of the Elevating Linear Fresnel Reflector (ELFR). The mirror elements rotate to reflect solar radiation to a secondary concentrator, but in contrast to a conventional LFR, the mirror elements are also adjustable in height to reduce shadowing and blocking of reflected rays.
- Fig. 2** Section view of the CPC cavity receiver.
- Fig. 3** The ELFR experimental equipment set-up for measuring an HTF's inlet and exit temperature.
- Fig. 4** An aerial view of the ELFR (left) and the illuminated receiver during operation (right).
- Fig. 5a-c** Experimental results showing the ELFR receiver achieving a steady state inlet and exit temperature for an average fluid temperature of (a) 33 °C (b) 40 °C and (c) 60 °C. The ambient and average cover glazing temperatures are also plotted.
- Fig. 6** The measured and estimated heat loss coefficient for the ELFR's receiver.
- Fig. 7a-c** Shows the ELFR receiving DNI and reaching a steady state exit temperature for an inlet temperature of (a) 38 °C (b) 45 °C and (c) 55 °C.
- Fig. 8** The measured and predicted exit temperatures for a range of inlet temperatures to the ELFR receiving DNI in the region of 750 W/m².
- Fig. 9** The optical efficiency estimate (based on measured thermal efficiency) and ray-tracing model prediction plotted against the transversal angle.
- Fig. 10** Measured inlet, exit, pipe and ambient temperature for determining the stagnation temperature at solar noon for a DNI of 760 W/m².
- Table 1:** Measured HTF exit temperatures and resulting thermal efficiencies for the ELFR receiving varying DNI and HTF inlet temperatures. The IAM dependant optical efficiencies based on the measured thermal efficiencies and heat loss coefficients are also tabulated.
- Table 2:** Predicted HTF exit temperatures and resulting thermal efficiencies for the ELFR receiving varying DNI and HTF inlet temperatures. The IAM dependant optical efficiencies based on a ray-tracing model and estimated heat loss coefficients are also tabulated.

References

- [1] Nixon J.D., Dey P.K., and Davies P.A., 2013, "Design of a novel solar thermal collector using a multi-criteria decision-making methodology," *Journal of Cleaner Production*, 59, pp. 150-159.
- [2] Singh P.L., Sarviya R.M., and Bhagoria J.L., 2010, "Heat loss study of trapezoidal cavity absorbers for linear solar concentrating collector," *Energy Conversion and Management*, 51, pp. 329-337.
- [3] Singh P.L., Sarviya R.M., and Bhagoria J.L., 2010, "Thermal performance of linear Fresnel reflecting solar concentrator with trapezoidal cavity absorbers," *Appl. Energy*, 87, pp. 541-550.
- [4] Singh P.L., Ganesan S., and Yadav G.C., 1999, "Technical note-Performance study of a linear Fresnel concentrating solar device," *Renewable Energy*, 18, pp. 409-416.
- [5] Khan M.K.A., 1999, "Technical note Copper oxide coatings for use in a linear solar Fresnel reflecting concentrating collector," *Renewable Energy*, 17, pp. 603-608.
- [6] Negi B.S., Mathur S.S., and Kandpal T.C., 1989, "Optical and thermal performance evaluation of a linear fresnel reflector solar concentrator," *Solar & Wind Technology*, 6, pp. 589-593.
- [7] Flores Larsen S., Altamirano M., and Hernández A., 2012, "Heat loss of a trapezoidal cavity absorber for a linear Fresnel reflecting solar concentrator," *Renewable Energy*, 39, pp. 198-206.
- [8] Yanhua L., Gu S., Mingxin L., Zhen D., Shuping C., and Chunyuan M., 2011, "Thermal performance analysis of linear fresnel reflector concentrator with a compound parabolic cavity absorber." *International Conference on Materials for Renewable Energy & Environment (ICMREE)*, 2011, pp. 168-172.
- [9] Reynolds D.J., Jance M.J., Behnia M., and Morrison G.L., 2004, "An experimental and computational study of the heat loss characteristics of a trapezoidal cavity absorber," *Solar Energy*, 76, pp. 229-234.
- [10] Burkholder F., and Kutscher C., 2009, "Heat Loss Testing of Schott's 2008 PTR70 Parabolic Trough Receiver," *NREL Report No. TP-550-45633*.
- [11] Facão J., and Oliveira A.C., 2011, "Numerical simulation of a trapezoidal cavity receiver for a linear Fresnel solar collector concentrator," *Renewable Energy*, 36, pp. 90-96.
- [12] Tesfamichael T., and Wäckelgård E., 2000, "Angular solar absorptance and incident angle modifier of selective absorbers for solar thermal collectors," *Solar Energy*, 68, pp. 335-341.
- [13] Konttinen P., Lund P.D., and Kilpi R.J., 2003, "Mechanically manufactured selective solar absorber surfaces," *Solar Energy Mater. Solar Cells*, 79, pp. 273-283.

- [14] Kennedy C.E., 2002, "Review of Mid- to High-Temperature Solar Selective Absorber Materials," NREL Report No. TP-520-31267.
- [15] Heimsath A., Platzer W., Bothe T., and Li W., 2008, "Characterization of Optical Components for Linear Fresnel Collectors by Fringe Reflection Method," 14th SolarPACES Conference, 4-7 March, 2008, Las Vegas, USA.
- [16] Peterka J.A., Sinou J.M., and Cernak J.E., 1980, "Mean Wind Forces on Parabolic - Trough Solar Collectors," NREL Report No. SR-550-32282.
- [17] Peterka J.A., Tan Z., Bienkiwicz B. and Cernak J.E., 1988, "Wind loads on heliostats and parabolic dish collectors," SERI Report No. STR-253-3431.
- [18] Peterka J.A., and Derickson R.G., 1992, "Wind load design methods for ground-based heliostats and parabolic dish collectors," Sandia National Laboratories Report No. SAND92-7009.
- [19] Hosoya N, Peterka J.A., Gee R.C., and Kearney D., 2008, "Wind tunnel tests of parabolic trough solar collectors, March 2001-August 2003," NREL Report No. SR-550-32282
- [20] Nixon J.D., and Davies P.A., 2012, "Cost-exergy optimisation of linear Fresnel reflectors," Solar Energy, 86, pp. 147-156.
- [21] Kalogirou S.A., 2004, "Solar thermal collectors and applications. Progress in Energy and Combustion Science," 30, pp. 231-295.
- [22] Duffie J.A., and Beckman W.A., 2006, "Solar engineering of thermal processes. 3rd ed," New York: John Wiley & Sons.
- [23] Morin G., Dersch J., Platzer W., Eck M., and Häberle A., 2012, "Comparison of Linear Fresnel and Parabolic Trough Collector power plants," Solar Energy, 86, pp. 1-12.
- [24] McIntire W.R., 1982, "Factored approximations for biaxial incident angle modifiers," Solar Energy, 29, pp. 315-322.
- [25] Nixon J.D., 2012, "Solar thermal collectors for use in hybrid solar-biomass power plants in India," Ph.D. dissertation, Aston University, UK.
- [26] Machine Building System Ltd., accessed June 18, 2014, <http://www.mbsitem.co.uk/>.
- [27] metoffice.gov.uk. Midlands: climate, accessed June 17, 2014, <http://www.metoffice.gov.uk/climate/uk/mi/print.html>.
- [28] Linak. Linear Actuator LA35, accessed June 17, 2014, <http://www.linak.co.uk/products/linear-actuators.aspx?product=LA35>.
- [29] Mathur S.S., Kandpal T.C., and Negi B.S., 1991, "Optical design and concentration characteristics of linear Fresnel reflector solar concentrators--II. Mirror elements of equal width," Energy Conversion and Management, 31, pp. 221-232.

[30] Welford W.T., and Winston R., 1989, "High collection nonimaging optics," San Diego: Academic Press.

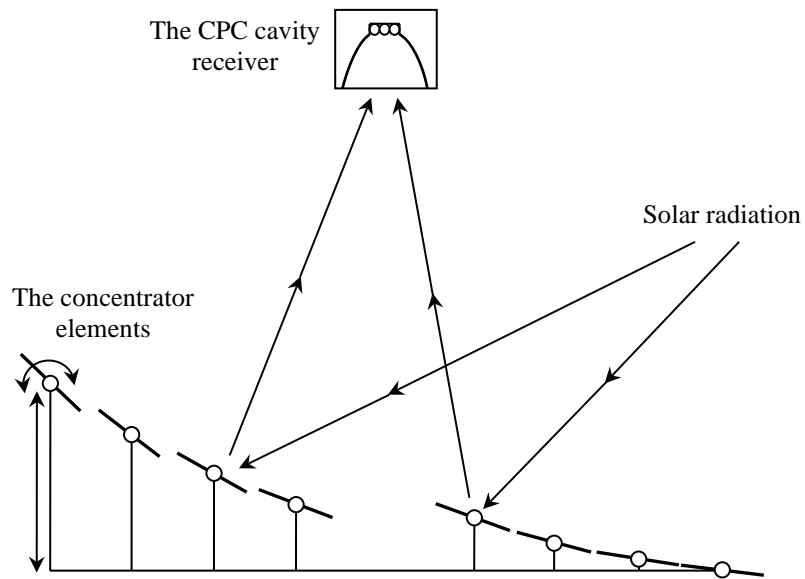


Figure 1

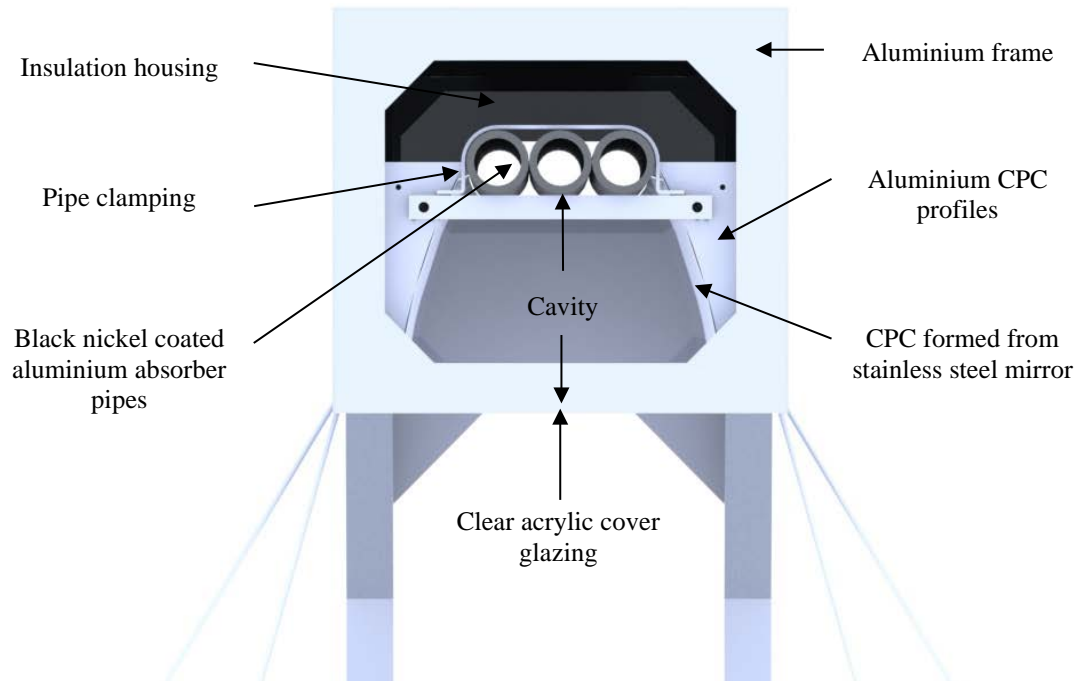


Figure 2

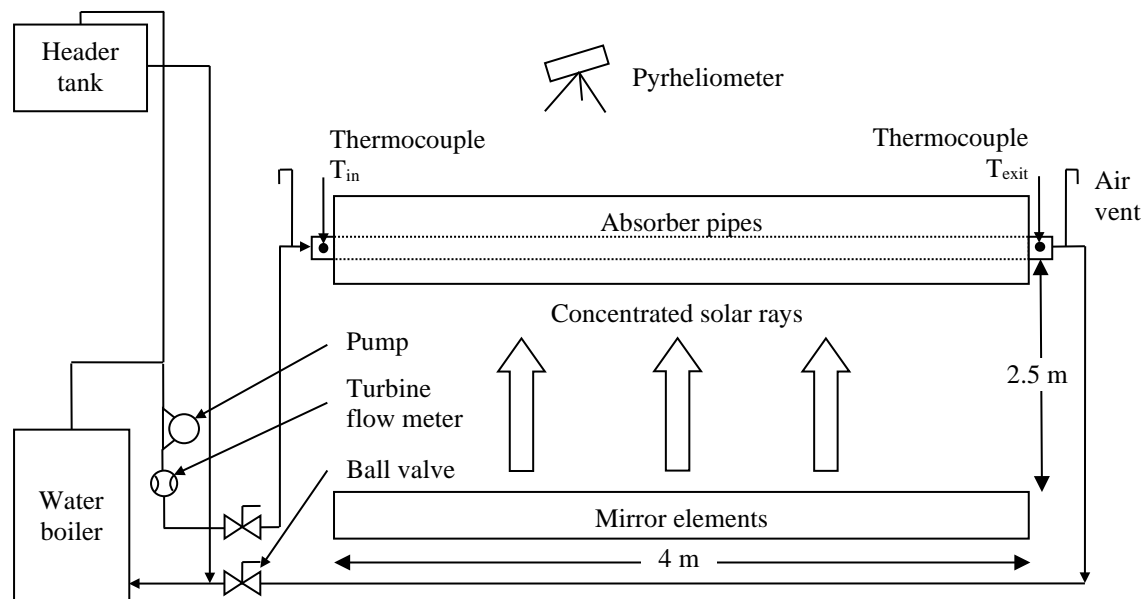


Figure 3



Figure 4

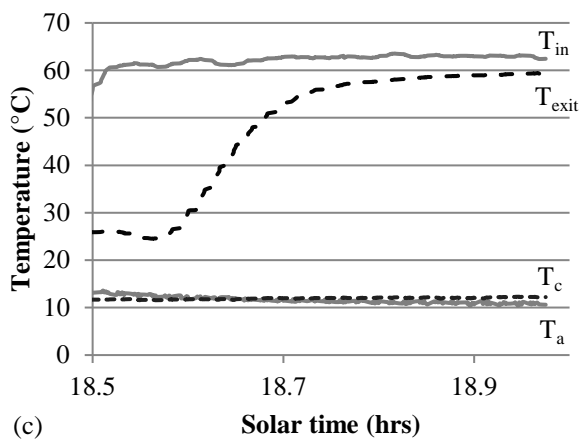
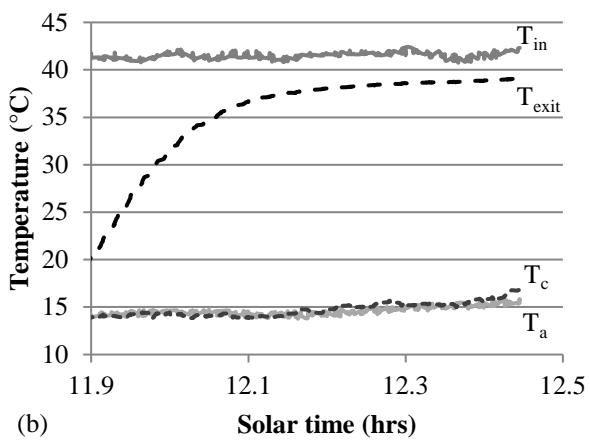
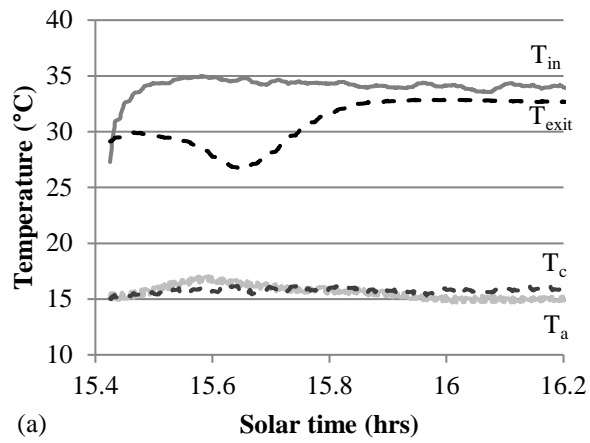


Figure 5a-c

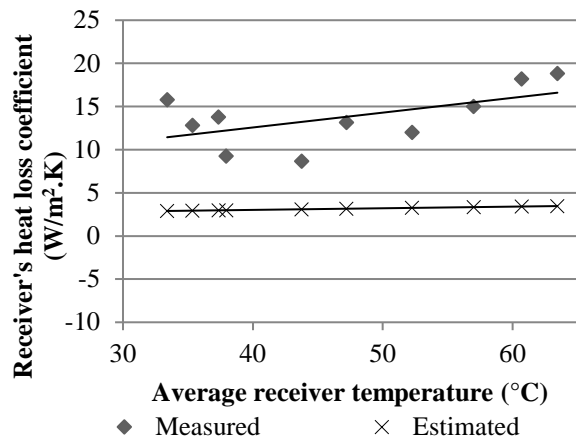
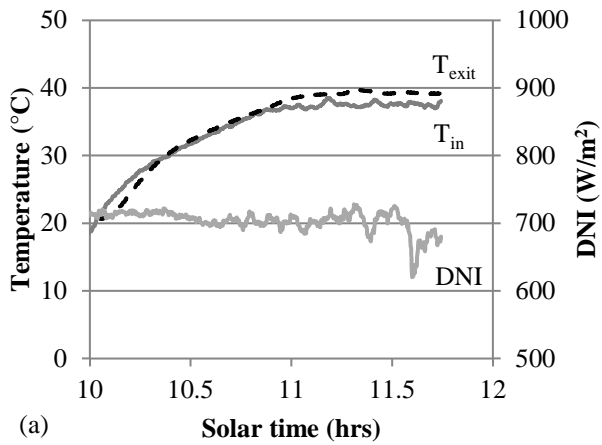
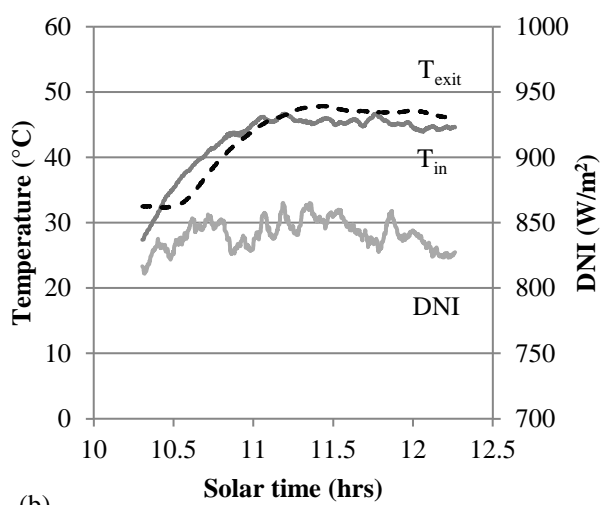


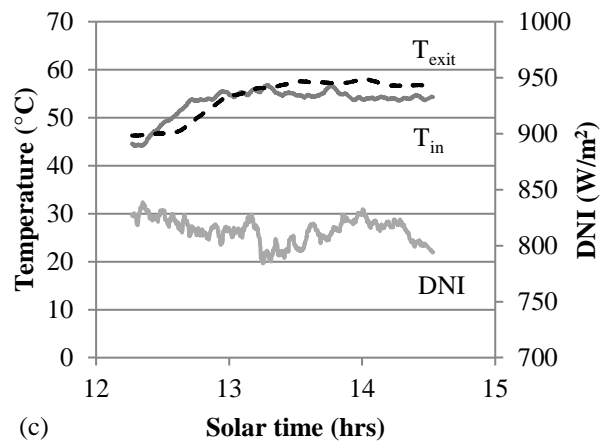
Figure 6



(a)



(b)



(c)

Figure 7a-c

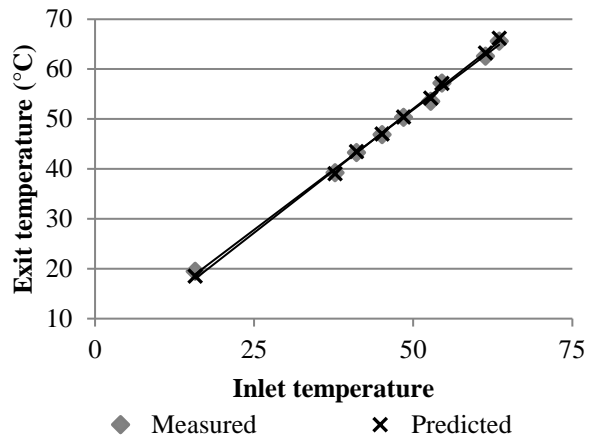


Figure 8

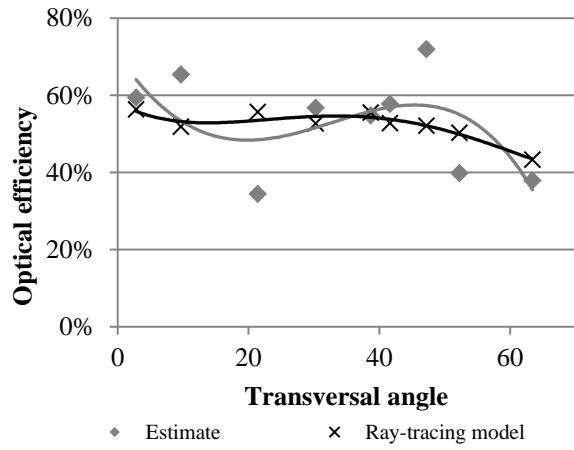


Figure 9

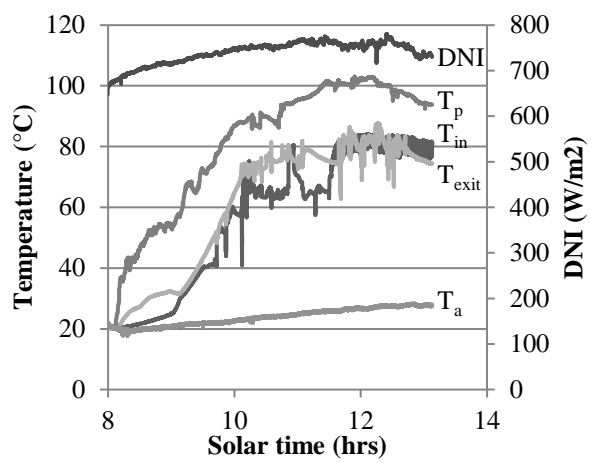


Figure 10